Acta Pharmaceutica Sinica B 2024;14(4):1742−1758

Chinese Pharmaceutical Association
Institute of Materia Medica, Chinese Academy of Medical Sciences

Acta Pharmaceutica Sinica B

www.elsevier.com/locate/apsb
www.sciencedirect.com

ORIGINAL ARTICLE

Novel Pt(IV) complex OAP2 induces STING activation and pyroptosis *via* mitochondrial membrane remodeling for synergistic chemo-immunotherapy

Renming Fan[a,b], Ruizhuo Lin[a,b], Shuo Zhang[c], Aohua Deng[a,b], Yongrui Hai[a,b], Junyan Zhuang[a,b], Yang Liu[c,*], Maosheng Cheng[c], Gaofei Wei[a,b,*]

[a]*Institute of Medical Research, Northwestern Polytechnical University, Xi'an 710072, China*
[b]*Research & Development Institute of Northwestern Polytechnical University in Shenzhen, Shenzhen 518057, China*
[c]*Key Laboratory of Structure-Based Drug Design and Discovery, Ministry of Education, School of Pharmaceutical Engineering, Shenyang Pharmaceutical University, Shenyang 110016, China*

Received 24 September 2023; received in revised form 7 November 2023; accepted 27 November 2023

KEY WORDS

Anti-tumor drug;
Prodrug;
Platinum;
Chemo-immunotherapy;
Mitochondrial membrane modeling;
STING;
Pyroptosis;
mtDNA

Abstract Mitochondrial membrane remodeling can trigger the release of mitochondrial DNA (mtDNA), leading to the activation of cellular oxidative stress and immune responses. While the role of mitochondrial membrane remodeling in promoting inflammation in hepatocytes is well-established, its effects on tumors have remained unclear. In this study, we designed a novel Pt(IV) complex, OAP2, which is composed of oxaliplatin (Oxa) and acetaminophen (APAP), to enhance its anti-tumor effects and amplify the immune response. Our findings demonstrate that OAP2 induces nuclear DNA damage, resulting in the production of nuclear DNA. Additionally, OAP2 downregulates the expression of mitochondrial Sam50, to promote mitochondrial membrane remodeling and trigger mtDNA secretion, leading to double-stranded DNA accumulation and ultimately synergistically activating the intracellular cGAS-STING pathway. The mitochondrial membrane remodeling induced by OAP2 overcomes the limitations of Oxa in activating the STING pathway and simultaneously promotes gasdermin-D-mediated cell pyroptosis. OAP2 also promotes dendritic cell maturation and enhances the quantity and efficacy of cytotoxic T cells, thereby inhibiting cancer cell proliferation and metastasis. Briefly, our study introduces the first novel small-molecule inhibitor that regulates mitochondrial membrane remodeling for

*Corresponding authors.
E-mail addresses: y.liu@syphu.edu.cn (Yang Liu), weigf0605@163.com (Gaofei Wei).

Peer review under the responsibility of Chinese Pharmaceutical Association and Institute of Materia Medica, Chinese Academy of Medical Sciences.

https://doi.org/10.1016/j.apsb.2023.11.032

active immunotherapy in anti-tumor research, which may provide a creative idea for targeting organelle in anti-tumor therapy.

1. Introduction

Mitochondria, known as the powerhouses of cells, play a crucial role in cell growth and various cellular processes[1−3]. They not only provide energy for cell growth but also contribute to cell differentiation, biogenesis, intercellular communication, generation of reactive oxygen species (ROS), and intracellular oxidative stress[4,5]. The unique structure of mitochondria, consisting of the inner mitochondrial membrane (IMM) and outer mitochondrial membrane (OMM), enables them to have diverse biological effects. In particular, the highly folded IMM facilitates the scope of enzymatic reactions and is enriched with complex enzymes involved in the mitochondrial respiration chain such as nicotinamide adenine dinucleotide-coenzyme Q oxidoreductase and cytochrome *c* oxidase[6]. In addition, mitochondria harbor their separate genomes known as mitochondrial DNA (mtDNA), which encode proteins essential for mitochondrial respiratory chain function and ATP production[7]. Dysregulation of mitochondrial function and mtDNA mutations have been implicated in various diseases, including cancer[8]. In tumor cells, there is a shift in cellular metabolism from oxidative phosphorylation to aerobic glycolysis, a phenomenon known as the Warburg effect[9]. This metabolic alteration leads to mitochondrial dysfunction and contributes to hypoxia induction and the activation of anti-apoptotic pathways[10,11]. These changes play critical roles in tumor progression, allowing cancer cells to evade the surveillance mechanisms of the body. Given the pivotal role of mitochondria in tumor development, targeting mitochondria to design anti-tumor drugs has gained significant attention in recent years[2,12−14].

Mitochondrial membrane remodeling, regulated by the OMM and IMM, is a crucial process involving mitochondrial fission and fusion[15,16]. It plays a pivotal role in maintaining cellular metabolism, regulating oxidative stress, and facilitating cellular growth, which is closely associated with various diseases. Mitochondrial membrane remodeling contributes to cellular adaption to diverse microenvironments and is controlled by intracellular signaling pathways to ensure the stability of the mitochondrial structure. Moreover, the release of cytokines during mitochondrial membrane rearrangement participates in key cellular processes such as differentiation and immune responses. Recent research has revealed that acetaminophen (APAP) can inhibit Sam50, a mitochondrial protein connecting the IMM and OMM, leading to mitochondrial membrane remodeling and mtDNA release. In hepatocytes, mtDNA released through mitochondrial membrane remodeling activates the intracellular STING pathway to promote inflammatory factor accumulation and induce liver injury[17]. However, the role of mitochondrial membrane remodeling in tumor cells remains largely unexplored. Based on this knowledge gap, we hypothesized that inducing mitochondrial membrane remodeling in tumor cells could increase mtDNA release, thereby improving the efficacy of anti-tumor immunotherapy.

Anti-tumor therapy has gradually evolved from "single medication and single mechanism" to "multi-mechanism combination therapy" as research into the causes and progression of tumors has progressed[18−22]. Platinum (Pt) chemotherapy drugs, commonly used as first-line anti-tumor treatments, exert their effects by inducing DNA damage and triggering apoptosis in cells by forming Pt-DNA complexes that target nuclear DNA[23−26]. This process can increase intracellular dsDNA content, activating the cGAS−STING axis, which is associated with the innate immune response[27]. Activation of this pathway results in the release of type I interferon (IFN) and other immune cytokines, promoting dendritic cell maturation and enhancing the quantity and function of cytotoxic T cells[28−31]. However, the efficacy of Pt chemotherapy drugs alone is limited due to the cellular self-protection mechanism. Recent studies have demonstrated that mtDNA can activate the host immune response of tumor cells by coordinating intracellular signaling pathways, including STING, and simultaneously triggering cellular inflammatory responses, promoting the expression of the NOD-like receptor protein (NLRP3) inflammasome[32,33]. Therefore, we hypothesize that amplifying the chemo-immunotherapeutic capacity of Pt drugs through mitochondrial membrane remodeling could eventually improve their anti-tumor effect.

In previous studies, we have been focused on modifying the structures of a series of Pt(IV) complexes to enhance their anti-tumor effects and mitigate potential side effects[34]. In this study, we designed and synthesized a novel Pt(IV) compound, OAP2 (Fig. 1A), by incorporating acetaminophen (APAP) into the central axis of oxaliplatin (Oxa). Our results proved that OAP2 exhibited significantly more potent cytotoxicity than Oxa, approximately 10-fold higher. Mechanistically, OAP2 targeted mitochondria, promoting mitochondrial membrane remodeling and facilitating the release of mtDNA into the cytoplasm. It also synergistically activated the cGAS-STING pathway by combining the nuclear DNA (ncDNA) generated from DNA damage (Fig. 1B). Moreover, OAP2-induced mitochondrial oxidative stress led to gasdermin-D (GSDMD)-mediated pyroptosis, enhancing the anti-tumor immune response. *In vivo* experiments using 4T1 tumor-bearing mice confirmed that OAP2 effectively enhanced the anti-tumor effect of Oxa, improved the immune response, increased infiltration of cytotoxic T cells, and successfully inhibited lung metastasis in breast cancer. Notably, when combined with immune checkpoint inhibitors (ICIs) αPD-L1, OAP2 showed simultaneous inhibition of primary and distant tumors, increasing tumor sensitivity to ICIs. In general, our findings provided novel insights into the activation of the STING pathway through mitochondrial membrane remodeling and offered a new strategy for designing anti-tumor drugs based on mitochondrial function to reverse the immunosuppressive microenvironment.

2. Results and discussion

2.1. Synthesis and characterization

To investigate whether the chemo-immunotherapeutic capacity of Oxa can be amplified by mitochondrial membrane remodeling, we designed and synthesized the compound OAP2. APAP an inhibitor

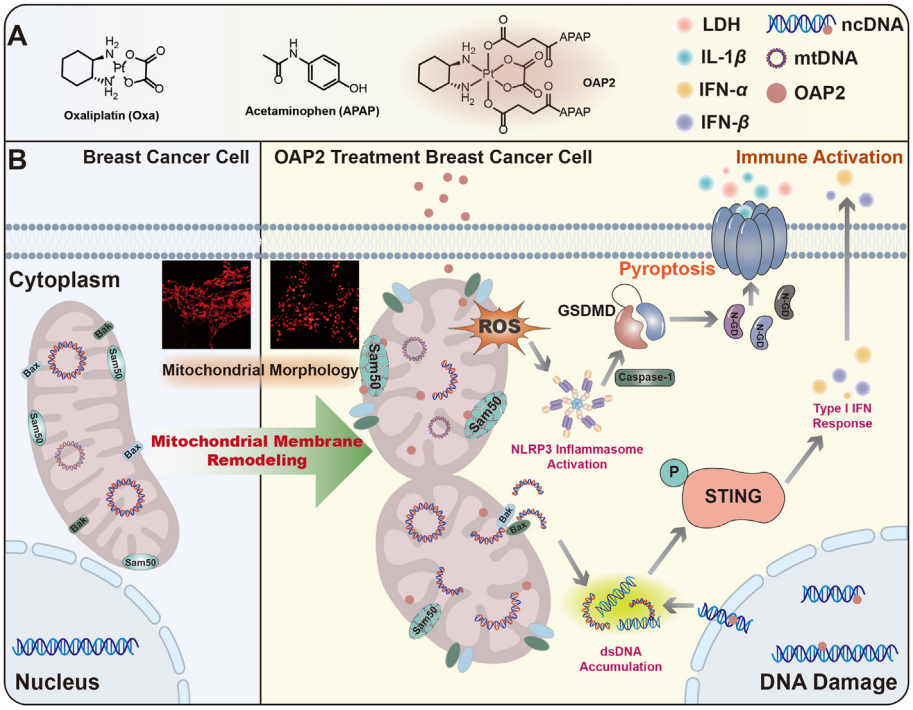

Figure 1 The novel Pt(IV) compound structure and expected mechanisms. (A) Chemical structure of Oxa, APAP, and OAP2; (B) The schematic illustration of OAP2 promoted mitochondrial membrane remodeling and facilitated the release of mtDNA into the cytoplasm.

of the mitochondrial protein Sam50, has been reported to induce mitochondrial membrane remodeling[17]. In this research, Oxa served as the structural backbone of OAP2, and two APAP molecules were added to the functional axis. We expected OAP2 could achieve improvement in chemo-immunotherapy through mitochondrial membrane remodeling.

The route of OAP2 synthesis is shown in Scheme 1. In brief, O-Oxa was prepared in H_2O_2 as previously reported. APAP-DC was synthesized *via* the esterification of APAP. Then, APAP-DC and O-Oxa were coupled in the presence of *N*,*N*-dimethylformamide (DMF), triethylamine (TEA) and *O*-(benzotriazol-1-yl)-*N*,*N*,*N*′,*N*′-tetramethyluronium tetrafluoroborate (TBTU) at room temperature. The crude product was purified using C18 column chromatography. The structure of OAP2 was characterized *via* ^{1}H, ^{13}C and ^{135}Pt-NMR, high-resolution mass spectrometry (HRMS), and HPLC analyses which are presented in the Supporting Information (Supporting Information Figs. S1−S5). These analytical data demonstrate that the two APAP molecules were successfully attached to the Oxa structure.

The stability of OAP2 in PBS was verified by HPLC, and the results are shown in Supporting Information Fig. S6, OAP2 could not be reduced in PBS in 72 h. The reduction rate of OAP2 reached 50% using ascorbic acid (10 mmol/L) as the reducing agent in 24 h (Supporting Information Fig. S7).

2.2. *Cytotoxicity of OAP2 in vitro*

To demonstrate the cytotoxicity of OAP2 *in vitro*, we conducted an MTT assay to evaluate its anti-tumor cell proliferation efficiency against 4T1 (breast cancer), B16F10 (melanoma), and Renca (kidney cancer) tumor cells. As shown in Table 1, OAP2 showed stronger cytotoxicity than Oxa and APAP across all three tumor cell lines. Especially, in 4T1 cells, the half-maximal inhibitory concentration (IC_{50}) value of OAP2 was 1.06 μmol/L, indicative of significantly higher activity than Oxa. The fold-

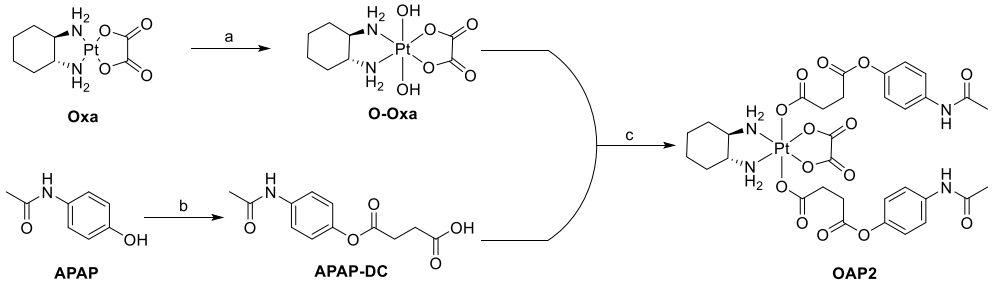

Scheme 1 Synthetic routine of platinum(IV) complex OAP2. Reagents and conditions: (a) H_2O_2, 75 °C, 5 h; (b) Dihydrofuran-2,5-dione, DAMP, THF, rt, 6 h; (c) TBTU, TEA, DMF, 60 °C, 48 h.

Table 1 IC_{50} values of different prototypical drugs and OAP2 to variable cell lines at 48 h[a].

Compound	IC_{50} (μmol/L)				
	4T1	B16F10	Renca	HUVEC	L-929
OAP2	1.06 ± 0.88	15.91 ± 2.48	13.11 ± 2.15	> 100	78.05 ± 0.77
Oxa	13.38 ± 0.66	25.89 ± 0.96	> 100	32.52 ± 2.01	44.57 ± 0.93
APAP	> 100	> 100	> 100	> 100	73.34 ± 0.88

[a]IC_{50} values are represented by mean ± SD of three independent experiments.

increase factor (FI), defined as the ratio of the IC_{50} value of Oxa to that of OAP2, was 12.64. We further evaluated the effects of OAP2 on the growth of L-929 and HUVECs. As shown in Table 1, Fig. 2A and Supporting Information Fig. S8, the cell viability (%) and vital cell staining using calcein-AM (c-AM), indicating that OAP2 has minimal impact on normal cells at its effective concentration.

Next, we proved that the cytotoxicity of OAP2 was credible. As shown in Supporting Information Fig. S9, the cells treated with OAP2 exhibited noticeable morphological deterioration, which was time-dependent. Additionally, colony formation experiments and wound healing assays were also performed to verify the ability of OAP2 on cell proliferation and metastasis (Fig. 2B and Supporting Information Figs. S10−S11). Compared with the control cells, the OAP2-treated cells showed significantly inhibited colony formation ability, and the cell migration rate decreased by approximately 20% at 48 h. The effects of the drug treatments were further confirmed throught live/dead cell staining (Supporting Information Fig. S12), where an increase in propidium iodide (PI, red fluorescence) staining indicated a higher number of dead cells in the OAP2 group.

To assess cell apoptosis, a common form of programmed cell death induced by chemotherapy, we employed Annexin-V/PI flow cytometry in 4T1 cells treated with different agents. As shown in Fig. 2D and Supporting Information Fig. S13, after 24 h of OAP2 incubation, the apoptosis rate in tumor cells exceeded 50%, which was significantly higher than that observed with Oxa and APAP at the same concentration. Moreover, we verified the expression of apoptosis-related proteins through Western blot experiment (Fig. 2C and Supporting Information Fig. S14). Consistent with previous experimental results, the expression of the apoptosis-promoting protein Bax was significantly upregulated in OAP2-treated cells, whereas the expression of apoptosis-inhibiting protein Bcl-2 was decreased. Furthermore, the level of Caspase-3, a key zymogen activated during apoptosis, also significantly increased after OAP2 treatment (Fig. 2C and F).

Finally, we utilized JC-1, a mitochondrial membrane potential probe, for flow cytometry and cell staining. In apoptotic cells, mitochondrial membrane potential decreased, causing a shift from red fluorescence to green fluorescence in the OAP2 group (Fig. 2E and Supporting Information Figs. S15−S16). These results provide further evidence that OAP2, as an excellent Pt(IV) compound, exhibits exceptional cytotoxicity and overcomes the defects of Pt(II).

2.3. *RNA-seq analysis*

To gain further insights into the cellular mechanisms affected by OAP2, we performed RNA-seq analysis on 4T1 cells treated with DMSO (control), Oxa, APAP, or OAP2 (2 μmol/L) for 24 h. As shown in Table S1, the average sequencing coverage of the DMSO (control), Oxa, APAP, and OAP2 treatment groups was 96.60%, 96.02%, 96.31%, and 96.46%, respectively. The correlation index between each sample was greater than 0.85 (Supporting Information Fig. S17), indicating the reliability and reproducibility of the data for further analysis. Gene Ontology (GO) enrichment analysis showed that OAP2 mainly affected biological processes, apoptotic processes, cytoplasmic and nuclear localization, as well as DNA and ATP binding (Supporting Information Figs. S18−S21). Kyoto Encyclopedia of Genes and Genomes (KEGG) enrichment analysis showed that OAP2 mainly influenced the TNF signaling pathway, NF-kappa B signaling pathway, mitogen activated protein kinase signaling (MAPK) pathway, and tyrosine metabolism in cancer (Fig. 3A and B). These results shed light on the specific molecular pathways and biological processes modulated by OAP2 treatment.

Gene set enrichment analysis (GSEA) revealed that, compared to the control and Oxa-treated groups, the OAP2-treated group exhibited decreased activity in DNA replication and the cell cycle (Fig. 3F−G, K−L). This reduction can be attributed to the release of intracellular Pt(IV) and it binding to dsDNA. Furthermore, GSEA also showed that the innate immune response, type-I IFN pathway, and tyrosine metabolism were enriched by OAP2-mediated chemo-immunotherapy (Fig. 3C−E, H−J). Based on the accumulating evidence, we hypothesized that OAP2 might play a key role in tumor suppression through the activation of the innate immune response.

2.4. *OAP2 induces mitochondrial membrane remodeling and STING activation*

An analysis of cellular RNA-seq data showed that OAP2 significantly activated the innate immune response of tumor cells compared to Oxa. However, the specific mechanism remained unclear. Mitochondria are bilayer membrane-structured organelles with a separate mtDNA genome, essential for maintaining normal cellular activities[35]. Recent studies have demonstrated that mtDNA serves as a key mediator of STING pathway activation[36−38]. Meanwhile, researchers found that APAP-induced mitochondrial membrane remodeling, through the downregulation of Sam50 and COX II expression in mitochondria, alters the mitochondrial bilayer structure while promoting the release of mtDNA into the cytoplasm[17]. Therefore, we hypothesized that OAP2 activates the STING pathway by inducing mtDNA release *via* mitochondrial membrane remodeling.

To support our hypothesis, we treated 4T1 cells with various drugs for 24 h. The results of the Western blot experiment are shown in Fig. 4A, Supporting Information Fig. S22A−B, and S23. The protein concentrations of Sam50 and COX II were significantly downregulated after APAP and OAP2 treatment, whereas Oxa had no significant effect. The mitochondrial apoptosis-associated protein Bax can translocate from the cytoplasm to the mitochondria after receiving a specific signal stimulus, forming a Bax/Bak macropore and promoting mtDNA

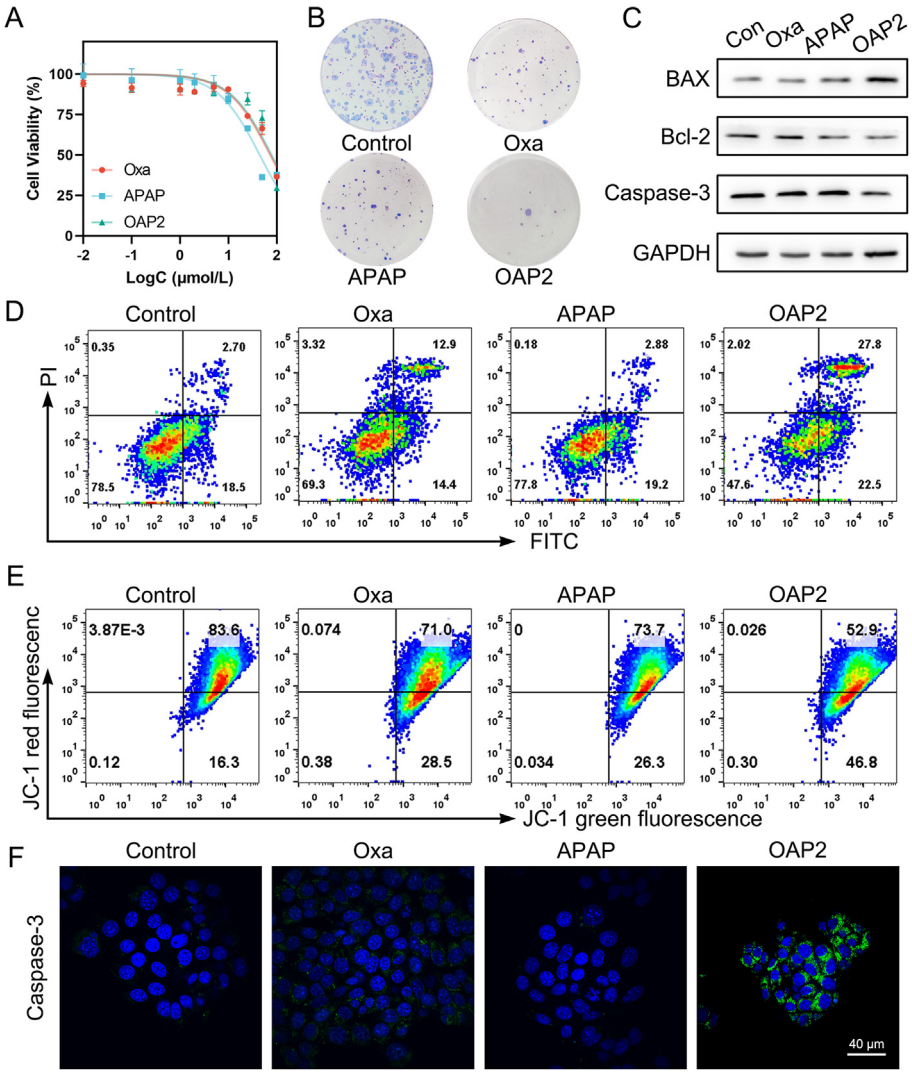

Figure 2 The Pt(IV) complex OAP2 *in vitro* anti-tumor activity. (A) The cell viability on the L-929 cell at different concentrations for 48 h; (B) Cell colony formation assay in the 4T1 cell; (C) Western blot images of cell apoptosis pathway protein in 4T1 cell line; (D) Flow cytometry analysis in the 4T1 cell stained with Annexin V-FITC and PI; (E) JC-1 flow cytometry analysis in the 4T1 cell; (F) Confocal images of the 4T1 intracellular active Caspase-3. Scale bars = 40 μm.

release[39]. After drug treatment for 24 h, the protein expression levels of Bax and Bak were significantly increased (Fig. 4B, Supporting Information Fig. S24). Co-localization immunofluorescence staining analysis of MitoTracker and Bax (Fig. 4C) also demonstrated the enrichment of pore formation by Bax in the mitochondria after drug treatment.

The deletion of Sam50 leads to mitochondrial membrane remodeling and mtDNA release. Compared to the control group, the mitochondrial exhibited a change in morphology from "filamentous" to "punctate," and the green fluorescence of DNA was observed to be released from the mitochondria into the cytoplasm (Fig. 4D). These observations provide evidence that drug administration resulted in mitochondrial membrane remodeling. In addition, we examined the protein content of the DNA damage marker γ-H2AX *via* Western blot experiment, and the results are shown in Supporting Information Fig. S25. The expression of γ-H2AX increased in 4T1 cells after Oxa and OAP2 treatment. The increase in both mtDNA and ncDNA induced activation of the STING pathway. We utilized Picogreen, a specific dye that selectively binds to dsDNA, resulting in green fluorescence (Supporting Information Fig. S26). We observed an increase in the OAP2 group, indicating elevated levels of dsDNA. Additionally, Western blot experiment (Fig. 4E−G, and Supporting Information Fig. S27) showed that compared to the control and Oxa groups, the expression of cGAS protein (a DNA sensor) was significantly increased in the OAP2 group. Moreover, phosphorylation levels of TANK binding kinase 1 (TBK1) protein and interferon regulatory factors (IRFs) were significantly upregulated in the OAP2 group. Immunofluorescence imaging of the p-STING protein (Supporting Information Fig. S28) further supported the activation of the STING pathway in 4T1 cells following OAP2 treatment.

Subsequently, the levels of IFN-α and IFN-β, released in the supernatant after different drug treatments, were measured *via* enzyme-linked immunosorbent (ELISA). After treatment with different drugs for 24 h, there was a significant increase in the contents of both IFN-α and IFN-β. In particular, compared to the control group, the OAP2 group showed 2.1- and 3.1-fold increases, respectively (Supporting Information Fig. S29). Collectively, in this section, we demonstrated that OAP2 could activate

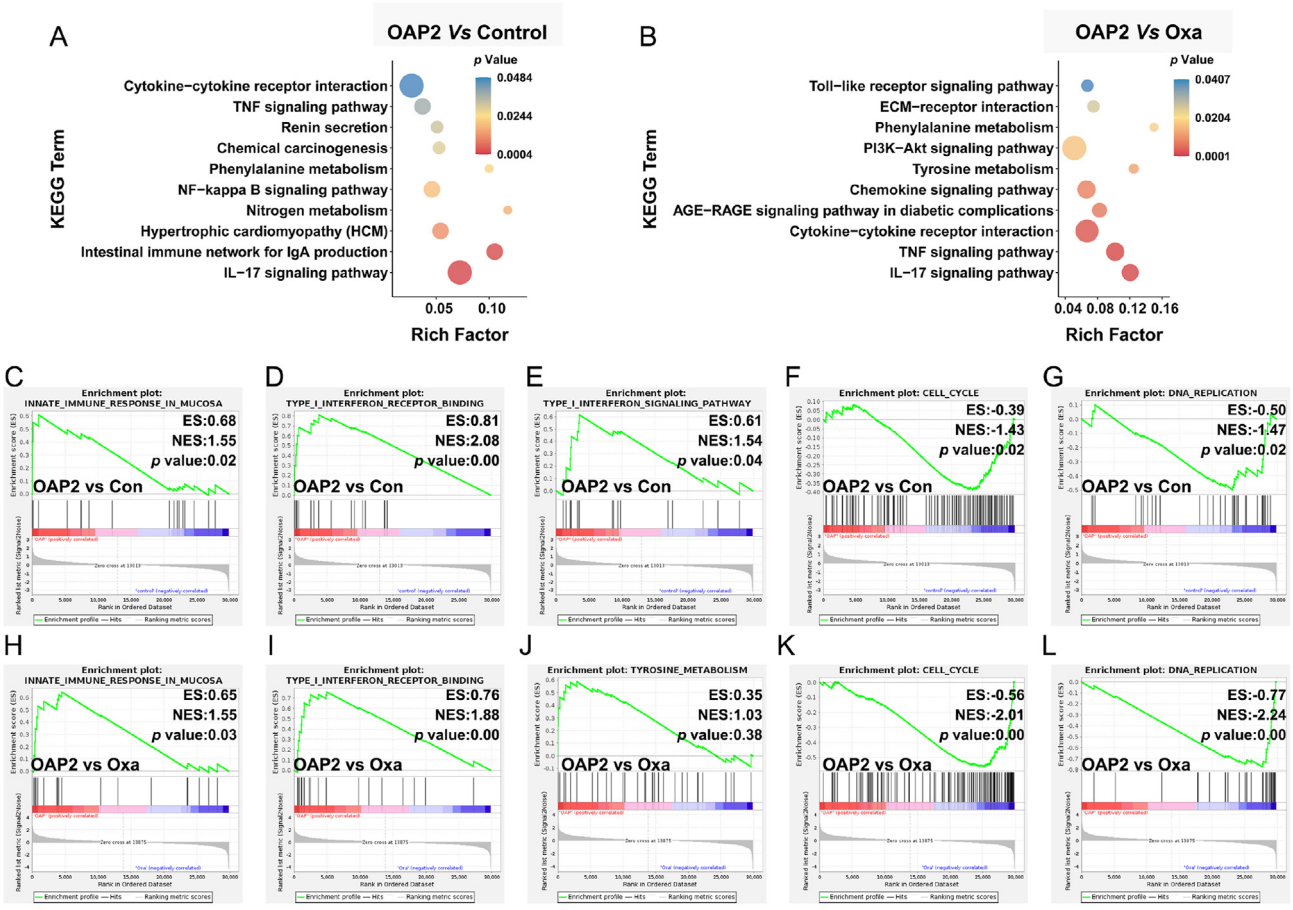

Figure 3 RNA-seq analysis result of the Pt(IV) complex OAP2 in 4T1 cell. (A−B) KEGG enrichment analysis of differentially expressed genes in OAP2 *vs* Con and OAP2 *vs* Oxa; (C−G) GSEA reveals various pathway enrichment of genes changed after OAP2-treated group *vs* Control group; (H−L) GSEA reveals various pathway enrichment of genes changed after OAP2-treated group *vs* Oxa group.

the intracellular innate immune response through multiple mechanisms (Fig. 4H). These include inhibiting the mitochondrial protein Sam50, which leads to mitochondrial membrane remodeling and the release of mtDNA. Additionally, OAP2 enhances the DNA damage-inducing capacity of Pt drugs, resulting in synergistic activation the cGAS-STING pathway and increasing release of the cytokines IFN-α and IFN-β.

2.5. *OAP2 induces oxidative stress and pyroptosis in vitro*

Glutathione (GSH), a scavenger of intracellular ROS, plays a crucial role in maintaining cellular redox homeostasis[40]. According to previous studies, it can serve as a reducing agent and simultaneously convert Pt(IV) compounds to Pt(II) to exert anti-tumor effects. Therefore, OAP2 is reduced to Oxa and APAP by intracellular GSH (Fig. 5A). APAP is activated by tyrosinase to form benzoquinone metabolites (AOBQ)[41,42]. The accumulation of large amounts of cytotoxic metabolites in the cells can further deplete GSH and produce ROS, ultimately leading to oxidative stress and cell death. To demonstrate the impact of OAP2 on GSH depletion and the induction of oxidative stress, we measured the total GSH content in 4T1 cells after drug administration *in vitro*. As shown in Fig. 5B, compared to APAP treatment alone, the intracellular GSH content was lower in the OAP2 treatment group, which was only 54.45% of that in the control group. A decrease in GSH content leads to an imbalance in cellular redox homeostasis and promotes cellular oxidative stress and mitochondrial damage. Consistently, we observed a significant increase in ROS production after OAP2 treatment, as tested using DCFH-DA (Fig. 5C and Supporting Information Fig. S30). This increase in ROS production was attenuated upon the addition of the ROS scavenger *N*-acetyl-L-cysteine (NAC). Mitochondria are the main organelles that produce ROS. Under conditions of oxidative stress, mitochondria morphology and distribution became disordered (Fig. 5E).

When observing the morphology of the cells after drug treatment, we unexpectedly discovered the presence of pyroptotic vesicles in dead cells after APAP and OAP2 treatment (Fig. 5D), demonstrating that OAP2 could induce cell death by triggering pyroptosis, in addition to cell apoptosis. According to previous studies, ROS produced by disordered mitochondria are the primary activators of the NLRP3 inflammasome, and mitochondria are vital for NLRP3 assembly. To determine whether activated NLRP3 mediates OAP2-induced pyroptosis, we first measured the NLRP3 protein content in 4T1 cells using Western blot experiment. As shown in Fig. 5F and Supporting Information Fig. S31A, compared to that in the control group, expression of the NLRP3 inflammasome was upregulated by approximately 1.2-fold in the APAP group; however, it was upregulated by approximately 1.7-fold in the OAP2 group. The NLRP3-mediated activation of caspase-1 induces the cleavage of GSDMD, resulting in the

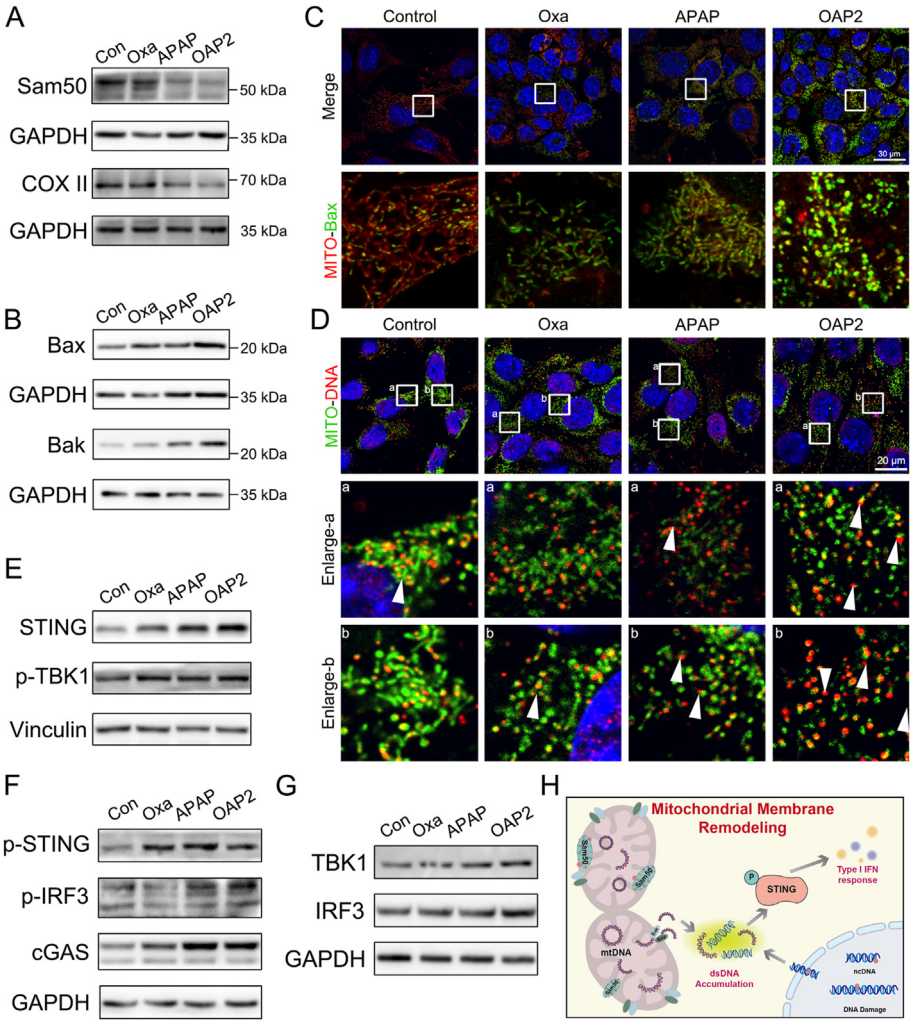

Figure 4 The Pt(IV) complex OAP2 induced mitochondrial membrane remodeling and activated the STING pathway *in vitro*. (A) The Western blot image of Sam50 and COX II protein in 4T1 cell line (n = 3); (B) The Western blot image of Bax and Bak in 4T1 cell line (n = 3); (C) Representative images of Bax-FTIC and MitoTracker™ Orange CMTMRos on 4T1 cells after various treatedments. Scale bars = 30 μm; (D) Representative images of DNA-Cy3 and MitoTracker™ on 4T1 cells after various treatedments. Scale bars = 20 μm; (E−G) The Western blot images of STING pathway related proteins in 4T1 cell line (n = 3); (H) Schematic illustration of OAP2-induced mitochondrial membrane remodeling to activate STING.

formation of membrane pores and pyroptosis. As shown in Fig. 5G and Fig. S31B−D, OAP2 increased the expression of cleaved GSDMD and cleaved-caspase-1 in 4T1 cells. Finally, we also detected the cytokines produced during the process of pyroptosis (Fig. 5H, and Supporting Information Fig. S32), including interleukin-1β (IL-1β) and lactic dehydrogenase (LDH). Compared to those in the control group, cytokine levels increased substantially after OAP2 treatment. In summary, OAP2 depletes GSH and increases ROS production, inducing oxidative stress and pyroptosis (Fig. 5I). The activated inflammasome NLRP3 recruits procaspase-1, promotes its transformation into active caspase-1, cleaves GSDMD proteins, and induces pyroptosis while producing large amounts of cytokines, such as IL-1β and LDH.

2.6. *Immune activation of OAP2 in vitro*

Immunotherapy, particularly immune checkpoint inhibitors (ICIs) targeting PD-1 and PD-L1, has emerged as a highly effective adjuvant therapy for various types of tumors[43,44]. However, the tumor immunosuppressive microenvironment always limits the clinical application of ICIs[45]. Both the intracellular innate immune STING pathway and pyroptosis can reverse the "cold" immunosuppressive microenvironment, tagging cells with an "eat me" signal and thus promoting DC maturation and T cell activation.

Next, we conducted a detailed analysis to investigate whether OAP2 could reverse immunosuppression in the tumor microenvironment. Damage-associated molecular patterns (DAMPs), including calreticulin (CRT), high-mobility histone B1 (HMGB1), and ATP, are highly expressed in immune-activated tumor cells and are secreted into the tumor microenvironment, enhancing immune cell recognition and cytotoxicity. Our results demonstrated a significant increase in CRT immunofluorescence intensity in the OAP2-treated group, as well as the release of HMGB1 and ATP into the cell supernatant (Fig. 6A−D). DCs, crucial antigen-presenting cells in innate and adaptive immunity, play an important role in immunotherapy. Mature DCs (mDCs) can recognize specific receptors on the surface of tumor cells and

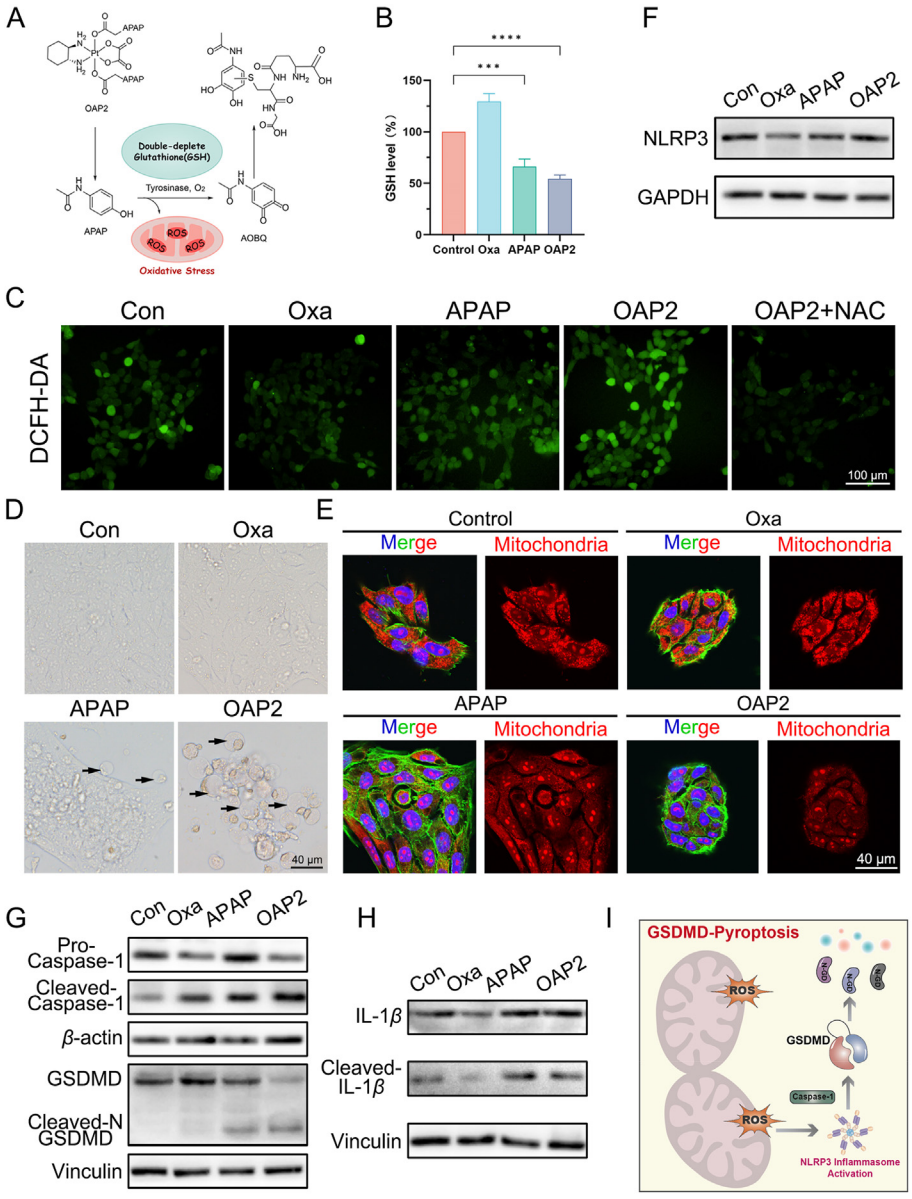

Figure 5 The Pt(IV) complex OAP2 induced oxidative stress and pyroptosis *in vitro*. (A) The scheme of OAP2 double-depleted GSH and generated ROS; (B) Intracellular GSH depletion after treated with Oxa, APAP, and OAP2 (2 μmol/L) for 24 h; (C) Representative images of intracellular ROS generation in 4T1 cells stained with DCFH-DA after various treatments. Scale bar = 100 μm; (D) Representative images of pyroptosis vesicles in the 4T1 cell treated with Oxa, APAP, and OAP2 (2 μmol/L) for 48 h. Scale bar = 40 μm; (E) Representative images of living cell mitochondria in the 4T1 cell treated with Oxa, APAP, and OAP2 (2 μmol/L) for 24 h. Blue: DAPI; Green: Alexa Fluor™ 488; Red: MitoTracker™ Orange. Scale bars = 40 μm; (F) Western blot image of NLRP3 protein in 4T1 cell line (n = 3); (G–H) Western blot image of pyroptosis related protein in 4T1 cell line (n = 3); (I) Schematic illustration of OAP2-induced pyroptosis.

present tumor antigens to cytotoxic T lymphocytes, thereby facilitating immune response activation. To evaluate the immunological effects of OAP2, we co-cultured bone marrow-derived DCs (BMDCs) with 4T1 cells treated with different drugs and analyzed them using flow cytometry. The expression of costimulatory molecules CD80 and CD86, representative markers of DC maturation, was significantly induced in the OAP2 group (21.1%) compared to the other groups (Fig. 6E and F). In general, this study demonstrated that OAP2 strengthened the immunogenicity of tumor cells by activating the STING pathway and promoting pyroptosis.

2.7. *In vivo anti-tumor efficacy study*

To evaluate the anti-tumor effect of OAP2 *in vivo*, we established a 4T1 cell-bearing BALB/c mouse model (Fig. 7A) and randomly divided them into five groups when the tumor volume grew to approximately 50 mm^3 on Day 7. Each group was treated with PBS (negative control), Oxa, APAP, Oxa + APAP, or OAP2. After 27 days, there was no significant difference in the relative tumor volume among the PBS, Oxa, and APAP groups (Fig. 7D and Supporting Information Fig. S33), which might be due to the low dose of APAP and drug resistance to Oxa. However, the

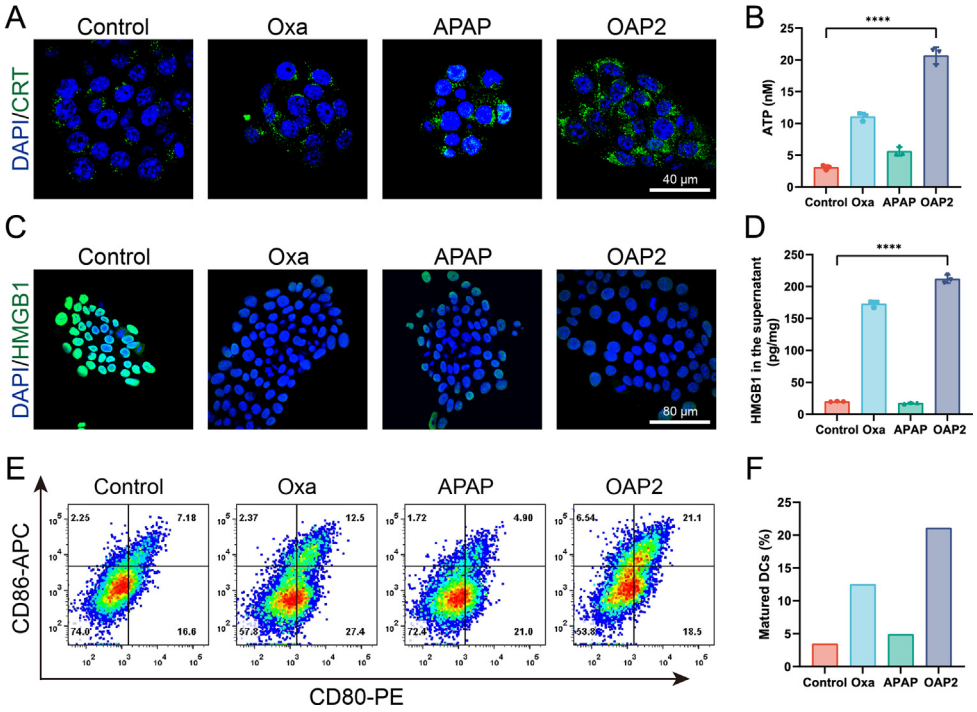

Figure 6 The Pt(IV) complex OAP2 induced immune activation *in vitro*. (A) Representative images of CRT generation on 4T1 cells after various treatedments. Scale bars = 40 μm; (B) ATP content released by 4T1 cells after incubation with Oxa, APAP, and OAP2 (2 μmol/L) for 24 h (n = 3); (C) Representative images of HMGB1 in 4T1 cells after various treatedments. Scale bars = 80 μm; (D) Quantification of the secretion of HMGB1 in 4T1 cell after incubation with Oxa, APAP, and OAP2 (2 μmol/L) for 24 h (n = 3); (E–F) The percentage of mature DCs was analysed by flow cytometry after co-culture with 4T1.

Oxa + APAP and OAP2 groups suggested better anti-tumor effects, with tumor volume reductions of 20.01% and 74.18%, respectively, compared with the PBS group. Particularly, the OAP2 group demonstrated a superior tumor inhibition effect, surpassing the combined administration group due to the structural stability of the drug. After 27 days, tumor size measurements (Fig. 7B and Fig. S30) confirmed that OAP2 exerted the strongest tumor inhibition effect (Fig. 7B and Supporting Information Fig. S34). Furthermore, there were no significant differences in the body weights of mice among the groups (Fig. 7C), indicating the safety of OAP2. Hematoxylin and eosin (H&E) staining of the main organs of the mice (Supporting Information Fig. S35) and routine blood analysis (Supporting Information Fig. S36) further supported the good biosafety profile of OAP2 with minimal side effects.

To further confirm the potential therapeutic effect *in vivo*, we performed H&E (Fig. 7E), Ki-67, and terminal deoxynucleotidyl transferase deoxyuridine triphosphate nick end labeling (TUNEL) staining of the tumor tissues. Ki67 is an important cell proliferation-related protein, and its expression is positively correlated with tumor growth. The OAP2 group exhibited significantly lower Ki67 protein expression compared to the other groups, indicating suppressed tumor cell proliferation (Fig. 7F). The TUNEL assay was used to detect apoptosis in tumor cells. OAP2 treatment led to increased apoptosis rates in tumor tissues compared to the control group (Fig. 7G), highlighting the potential of OAP2 as a prodrug compound for inhibiting *in vivo* tumor growth. Specifically, it induces apoptosis and inhibits tumor cell proliferation *in vivo*.

2.8. *In vivo immune activation*

Based on the encouraging results of the immune activation assays *in vitro*, we evaluated the systemic anti-tumor immunity induced by OAP2 *in vivo* in an *in vivo* setting using the 4T1 breast tumor model. Flow cytometry, immunofluorescence staining, and ELISA were employed to determine immunological indicators.

mDCs are essential for *in vivo* immunity as they promote T cell proliferation and activation through antigen presentation. As shown in Fig. 8A–D and Supporting Information Fig. S37, flow cytometry analysis of mDC populations in the spleen, tumor-draining lymph nodes, and tumor tissues revealed the highest mDC content in these three tissues after OAP2 treatment (23.2% in the spleen, 59.2% in the tumor, and 36.7% in the lymph nodes). In addition, ELISA analysis of pro-inflammatory cytokines, including IL-12, TNF-α, and IFN-α in the tumor tissues, showed a significant increase in cytokine secretion in the OAP2 group, with 2.5-, 3.0-, and 2.4-fold increases, respectively, compared to that in the PBS group (Fig. 8G and H).

Previous studies have demonstrated that both STING and cell pyroptosis can activate T cell proliferation and promote their infiltration into tumor tissues. Therefore, we collected T cells from the tumor tissues and spleens of the mice for flow cytometric analysis. As shown in Fig. 8E and F and Supporting Information Fig. S38, compared to the PBS group, OAP2 treatment significantly increased the proportions of $CD3^+CD8^+$ T cells and $CD3^+CD4^+$ T cells in the tumor tissue ($CD3^+CD8^+$ T cells: 13.6%; $CD3^+CD4^+$ T cells: 6.73%) and spleen ($CD3^+CD8^+$ T cells: 9.32%; $CD3^+CD4^+$ T cells: 25.7%). Moreover, the effect of

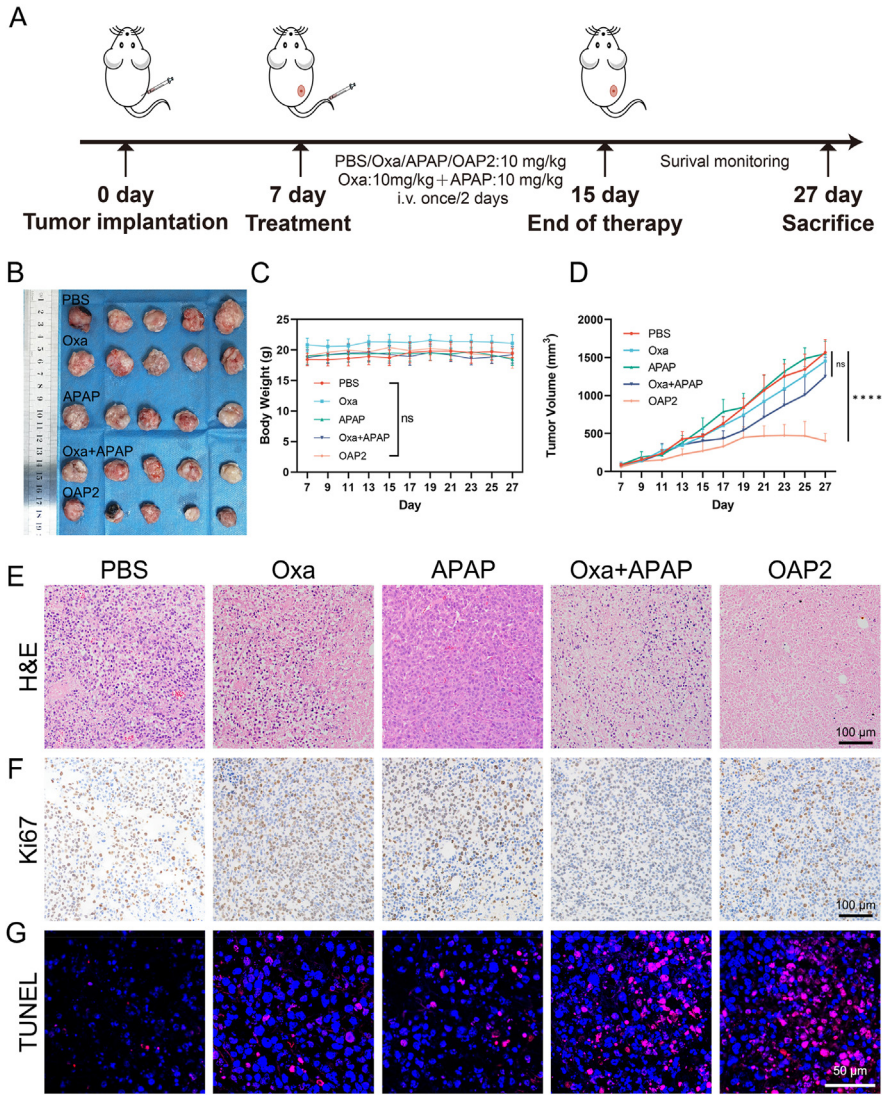

Figure 7 Anti-tumor effects of OAP2 *in vivo*. (A) Schematic representation of the OAP2 anti-tumor efficacy 4T1 subcutaneous tumor-bearing model; (B) Pictures of tumors in each group of mice at the end of the experiment; (C) Statistical analysis of body weight fluctuation of mice during the experiment. (D) Statistical analysis of tumor volume of mice during the experiment; (E) Representative picture of H&E staining of tumor tissue. Scale bars = 100 μm; (F) Representative picture of Ki67 staining of tumor tissue. Scale bars = 100 μm; (G) Representative picture of TUNEL staining of tumor tissue. Scale bars = 50 μm.

OAP2 was notably superior to that of Oxa and APAP treatment alone.

In addition to activated immune cells, the tumor microenvironment is composed of a large population of immunosuppressive cells, such as tumor-associated macrophages (TAMs). M1-type macrophages, which express CD86, are capable of releasing pro-inflammatory cytokines to clear tumor cells. In contrast, $CD206^+$ M2-type macrophages release immunosuppressive factors (such as IL-10, TGF-β, etc.) to promote tumor progression. Analysis of the proportions of M2 and M1 macrophages in the tumor microenvironment showed that Oxa or OAP treatment reversed immunosuppression, resulting in decreased levels of immunosuppressive factors IL-10 and TGF-β (Fig. 8J−K and F Supporting Information Fig. S39). Finally, immunofluorescence staining for p-STING proteins in tumor tissues and quantitative ELISA analysis of IL-1β, IFN-α, and IFN-β levels confirmed that OAP2 treatment induced STING pathway activation and cell pyroptosis *in vivo* (Fig. S40 and Fig. 8L−N). In conclusion, this section demonstrated that OAP2 could induce STING activation and cell pyroptosis *in vivo*, enhancing immune cell infiltration and switching the tumor microenvironment from "cold" to "hot."

2.9. *Inhibition of tumor metastasis in vivo*

Metastasis to multiple organs is a major contributor to the poor prognosis and mortality of advanced breast cancer patients. Effective inhibition of tumor cell dissemination and growth at distant sites from the primary tumor is a critical challenge in clinical practice. In our previous experiments, we showed that the compound OAP2 effectively inhibited the migration of 4T1 cells in a 2D wound healing assay *in vitro*. Buiding upon this strong evidence, in this part, we designed and conducted two mouse metastasis models to investigate the inhibitory effect of OAP2 on tumor metastasis *in vivo* (Fig. 9A and Supporting Information Fig. S41). The mouse tumor model of lung metastasis was

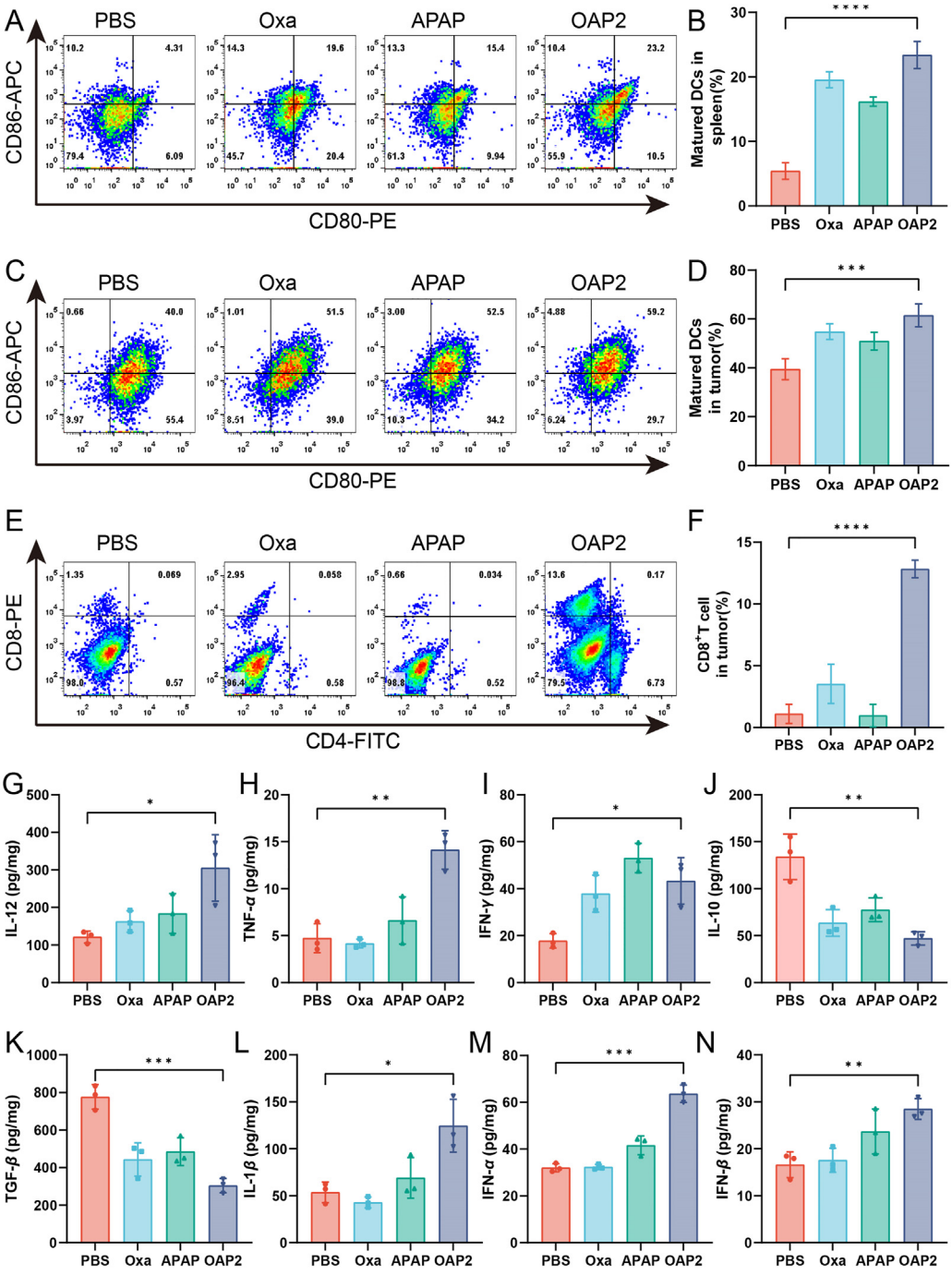

Figure 8 The immune activation effect of OAP2 *in vivo*. (A−B) Analysis of mature DC cells in mouse spleen. Expression of CD80 and CD86 quantitatively detected by flow cytometry (A), and statistical analysis (B). (C−D) Analysis of mature DC cells in mouse tumor site. Expression of CD80 and CD86 quantitatively detected by flow cytometry (C), and statistical analysis (D). (E−F) Analysis of cytotoxic T cells in mouse tumor. Expression of CD4 and CD8 quantitatively detected by flow cytometry (E), and statistical analysis (F). (G−N) Tumor tissue cytokine expression content measured by ELISA ($n = 3$).

established *via* the intravenous injection of 1×10^5 4T1 tumor cells on the 7th day before drug treatment. The mice were randomly divided into four groups, and the *in situ* tumor volume and body weight were recorded throughout the treatment period (Fig. 9B and Supporting Information Fig. S42). Lung tissues were collected at the end of the treatment on the 16th day and H&E staining was performed. Remarkably, OAP2 treatment led to a significant reduction in the number of lung metastatic nodules in mice (Fig. 9C). The emergence of ICIs has alleviated the clinical problem of immunosuppression; however, as their application has broadened, the average response rate of patients to ICIs is only 26%, and most patients cannot achieve the desired therapeutic effect owing to drug resistance and immunosuppression. Therefore, we investigated the combination of OAP2 with αPD-L1

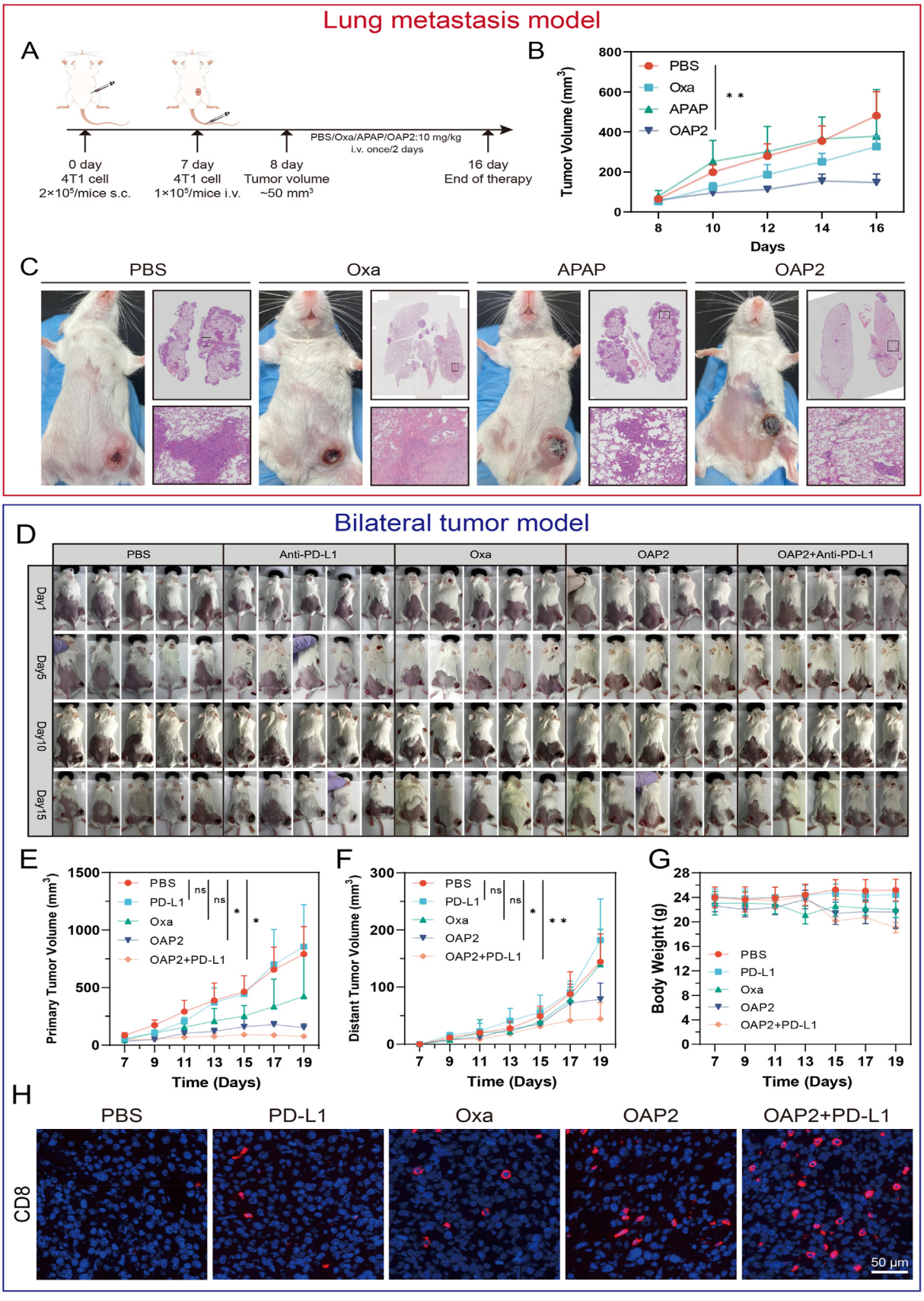

Figure 9 Anti-tumor metastatic effects of OAP2 *in vivo*. (A) Schematic representation of the OAP2 anti-tumor efficacy on 4T1 lung metastasis model; (B) Statistical analysis of tumor volume of mice during the experiment ($n = 5$); (C) Representative pictures of mice at the end of treatment and H&E staining of lung; (D) Representative pictures of mice during treatment of bilateral tumor models; (E−F) Statistical analysis of tumor volume of primary (E) and distant (F) tumors in the bilateral tumor model during the experiment ($n = 5$); (G) Changes of mouse body weight during the experiment of 4T1 bilateral tumor model ($n = 5$); (H) Representative picture of CD8 staining of tumor tissues. Scale bars = 50 μm.

therapy to determine whether it could reverse drug resistance and prevent distant metastasis using a bilateral tumor model (Fig. 9D). Notably, the combination treatment resulted in inhibited growth of both primary and distant tumors (Fig. 9E−G, and Supporting Information Fig. S43). Immunofluorescence staining of distant tumors at the end of treatment clearly revealed enhanced infiltration of $CD8^+$ T cells in the combination treatment group (Fig. 9H). Collectively, these findings confirmed that OAP2 could effectively inhibit lung metastasis and improve the sensitivity of tumors to αPD-L1 therapy. The combination of OAP2 with immunotherapy holds promise for overcoming drug resistance and preventing distant metastasis in breast cancer.

3. Conclusions

Mitochondria, as the energy sources of the cells, play a crucial role in maintaining cell growth and proliferation. Their structure and function are vital for cellular metabolism. Mitochondria have their own independent genome, known as mtDNA, which encodes proteins associated with the mitochondrial respiratory chain. While the effect of mitochondrial membrane remodeling on tumor progression remains unclear, previous studies have shown that mitochondrial membrane remodeling caused by Sam50 deletion in hepatocytes can lead to mtDNA release, activation of the cGAS-STING signaling pathway, and acute liver injury. To fill the gap in anti-tumor research related to mitochondrial membrane remodeling, we designed and synthesized a novel Pt-APAP complex called OAP2. By downregulating Sam50 expression, OAP2 promoted mitochondrial membrane remodeling in tumor cells, activating the STING signaling pathway and ultimately reversing the immunosuppressive tumor microenvironment.

From the experimental results, OAP2 possesses outstanding anti-tumor activity *in vitro*. RNA-seq analysis showed significant activation of the innate immune response and the type-I IFN pathway after OAP2 treatment, surpassing the activation observed in the control and Oxa groups. Mechanistically, we proved that compound OAP2 could promote mitochondrial membrane remodeling by downregulating Sam50 protein expression, facilitating the recruitment of Bax proteins to create pores in the mitochondrial membrane, resulting in increased mtDNA release. Meanwhile, OAP2-induced mitochondrial oxidative stress promoted the formation of the NLRP3 inflammasome, which facilitated GSDMD-mediated pyroptosis through the activation of caspase-1 maturation. Both the STING pathway activation and pyroptosis could reverse the immunosuppressive tumor microenvironment. However, in the future, we need to delve deeper into the intricate mechanisms responsible for OAP2's induction of mitochondrial membrane remodeling and activation of the STING pathway.

Encouraged by the excellent anti-tumor activity *in vitro*, we proceeded to evaluate the anti-tumor effect and biosafety of OAP2 on 4T1 tumor model *in vivo*. Flow cytometry analysis and ELISA measurements of immune cells and anti-tumor cytokines in the tumor microenvironment demonstrated that OAP2 promotes DC maturation and infiltration of cytotoxic T cells while significantly increasing the levels of anti-tumor immune factors. These results demonstrate that OAP2 facilitates the transition from a "cold" to a "hot" tumor microenvironment. Furthermore, in the tumor metastasis models, OAP2 effectively reduced the number of lung nodules and enhanced the sensitivity of immune checkpoint inhibitors.

In summary, this study designed a platinum prodrug, OAP2, utilizing the clinically safe drug APAP as its ligand, positions OAP2 as an ideal candidate for clinical translation. Currently, the majority of platinum-based prodrugs that activate the cellular STING pathway are administered in nanoparticulate form. In contrast, our OAP2, with its small molecule structure, provides the benefits of predictability and controllability, streamlining drug delivery considerations. OAP2 introduces an innovative mechanism for STING activation, achieved through the promotion of mitochondrial membrane remodeling, mtDNA release, and the induction of oxidative stress and pyroptosis. This multifaceted approach significantly enhances STING pathway activation, creating an immunostimulatory tumor microenvironment. These findings provide novel insights and open up new avenues for the design of anti-tumor drugs targeting mitochondrial function.

4. Experimental

4.1. Chemicals and materials

All commercial reagents were used without purification unless otherwise specified. Oxaliplatin (Oxa) was purchased from Energy Chemical Co., Ltd., China. Other chemicals and chemical solvents were purchased from AdamasBeta. HPLC chromatograms (semi-preparation) were obtained using a Thermo Scientific Dionex UltiMate 3000 system equipped with a reverse-phase column (Prep-C18, Agilent) measuring 250 mm × 21.2 mm. The mobile phase consisted of a mixture of acetonitrile and 0.1% TFA water in a 50:50 ratio. The flow rate was set at 10.0 mL/min, and peak detection was performed at 254 nm under UV light. An injection volume of 1.0 mL and an injection time of 40 min were used for each analysis. NMR spectra were recorded on a Bruker ARX 600 MHz spectrometer. Chemical shifts were reported in parts per million (ppm), and coupling constants (J) were given in hertz (Hz). High-resolution mass spectrometry (HRMS) was performed on a Waters Xevo G2-XS Tof instrument. Elemental analysis data were obtained using an Elementar UNICUBE element analyzer.

4.2. Synthesis and characterization

Oxaliplatin (1000 mg, 2.52 mmol) was suspended in a mixture of hydrogen peroxide (30%, 30 mL) and heated to 75 °C for 6 h. The resulting mixture was then cooled to 4 °C overnight, resulting in the formation of a light-green precipitate. The precipitate was collected through centrifugation and washed three times with water. The resulting product, O-Oxa, was obtained as a powder (621.3 mg, yield = 57.23%).

Acetaminophen (500 mg, 3.31 mmol) and dihydrofuran-2,5-dione (661.99 mg, 6.62 mmol, 2.0 equiv) were dissolved in 20 mL of tetrahydrofuran. A catalytic amount of DMAP (0.02 mg) was added, and the mixture was stirred at room temperature for 6 h. After completion of the reaction, the solvent was removed by vacuum distillation. The residue was cooled to room temperature, and an appropriate amount of sodium bicarbonate ($NaHCO_3$) solution was added to dissolve the residue and remove impurities. The resulting solution was extracted with ether, and the pH of the aqueous layer was adjusted to 4. White crystals were precipitated, which were then filtered, dried, and APAP-DC obtained as white products (591.78 mg, yield = 71.23%).

Next, O-Oxa (200.0 mg, 0.46 mmol), APAP-DC (349.47 mg, 1.39 mmol, 3.0 equiv), TBTU (446.33 mg, 1.39 mmol, 3.0 equiv),

and TEA (0.19 mL, 1.39 mmol, 3.0 equiv) were mixed in 8.0 mL of dimethylformamide (DMF). The reaction mixture was vigorously stirred at room temperature for 48 h. Unreacted O-Oxa was removed by filtration, and the mixture was further purified using C18 column chromatography with a mixture of methanol and water in a 1:1 ratio as the eluent. Yellow powder of OAP2 was obtained with a reasonable yield (193.57 mg, yield = 46.50%, purity >95% by HPLC).

^{1}H NMR (500 MHz, DMSO-d_6) δ 9.99 (s, 2H), 8.50−8.06 (m, 4H), 7.69−7.50 (m, 4H), 7.13−6.96 (m, 4H), 2.84−2.62 (m, 8H), 2.54 (s,2H), 2.04 (s, 8H), 1.41−1.29 (m, 4H), 1.09−0.83 (m, 2H).^{13}C NMR (126 MHz, DMSO) δ 181.66, 171.92, 167.54, 163.90, 148.07, 134.63, 121.88, 120.16, 61.79, 31.36, 30.94, 30.12, 24.88, 23.78. ^{195}Pt NMR (86 MHz, DMSO) δ 1621.45; HRMS (ESI): calcd for $[M + Na]^+$ $C_{32}H_{38}N_4NaO_{14}Pt$, 920.1930; found, 920.1934. Elemental analysis calculated for $C_{32}H_{38}N_4O_{14}Pt$: C 41.97%, H 4.40%, N 6.12%; Found: C 41.80%, H 4.32%, N 5.98%.

4.3. Cell lines and cell culture

4T1 (murine breast cancer cells), B16F10 (murine melanoma cells), Renca (murine renal carcinoma cells), and PUMC-HUVEC-T1 (human endothelial cell) were purchased from Procell Life Science&Technology Co., Ltd. L-929 (murine fibroblast) was purchased from Wuhan Servicebio Technology Co., Ltd. All the cells were cultured in the DMEM/RPMI-1640/MEM culture medium (Sangon Biotech (Shanghai) Co., Ltd., E600003, and E600028) with 10% FBS (Excell Bio, Shanghai, FSP500) and 1% penicillin-streptomycin (MacGene, Beijing, CC004). In addition, an additional 1 mmol/L sodium pyruvate (Sangon Biotech (Shanghai) Co., Ltd., A600884) and 2 mmol/L L-glutamine (Sangon Biotech (Shanghai) Co., Ltd., A100374) were added to the Renca medium.

The cells utilized in the experiments were cultured in the carbon dioxide cell culture box (Thermo Fisher-Forma 371) with 5% CO_2 at 37 °C.

4.4. Animals

Healthy BALB/c female mice (6−8 weeks, 18−20 g) were purchased from Charles River, Beijing. All the animals were raised in a free of pathogens cage. The temperature was kept at 21 ± 2 °C, and the relative humidity was maintained at 40%−70% with a 12 h light/dark cycle. All animal experiments were conducted under the guidelines of the Institutional Animal Care and Use Committee at Northwestern Polytechnical University.

4.5. Cytotoxicity

4T1, B16F10, Renca, L-929 and HUVEC cells were seeded in the 96-well (Guangzhou Jet Bio-Filtration Co., Ltd., TCP001096) until reaching a confluency of approximately 50%, followed by treatment with various drugs. DMSO, Oxa, APAP, and OAP2 were treated for 48 h at different concentrations. After drug incubation, the medicated medium was removed and 200 μL MTT (Beyotime Biotechnology, ST1537) working solution was added to each well and incubated at 37 °C for 4 h. Finally, the MTT solution was removed and 200 μL DMSO was added to dissolve the precipitation. The results were analyzed by a microporous plate multifunctional detector (Tecan−Tecan Spark, Switzerland).

4.6. Live and dead cell staining

Calcein/PI Cell Viability/Cytotoxicity Assay Kit was purchased from Beyotime Biotechnology (C2015S) to measure the cell cytotoxicity of 4T1 and HUVEC cells. Cells were seeded in the 12-well plates (Guangzhou Jet Bio-Filtration Co., Ltd., TCP001012) until reaching a confluency of approximately 70%, followed by treatment with various drugs. DMSO (2 μmol/L), Oxa (2 μmol/L), APAP (2 μmol/L), OAP2 (2 μmol/L) were treated for 24 h. After drug incubation, staining was performed according to the protocols and the results were analyzed by the confocal laser scanning microscope (CLSM, OLYMPUS−OLYMPUS FV3000).

4.7. Colony-forming assay

A colony formation assay is designed to test the ability of drugs to suppress the cells. 1×10^3 cells per well were cultured in a 6-well plate (Guangzhou Jet Bio-Filtration Co., Ltd., TCP001006). After treating the cells with DMSO (2 μmol/L), Oxa (2 μmol/L), APAP (2 μmol/L), OAP2 (2 μmol/L) for 24 h, the treatments were removed the and replaced with 1640 medium. The cells were then cultured for 10−14 days. Afterward, the medium was removed, and the cells were stained with crystal violet (Beyotime Biotechnology, C0121).

4.8. Wound healing assay

Cells were cultured in a 6-well plate and incubated overnight. The scratched wound was generated by a sterile 200 pipette tip. Subsequently, the cells were washed three times with PBS and the medium was replaced with DMSO (2 μmol/L), Oxa (2 μmol/L), APAP (2 μmol/L), and OAP2 (2 μmol/L). Photographs of the cells were taken at 0, 24, and 48 h. Finally, the wound area was calculated using Image J software.

4.9. Apoptosis assay

To measure cell apoptosis induced by OAP2, 4T1 cells were seeded in a 6-well plate and incubated overnight until reaching a confluency of approximately 70%. Subsequently, the cells were treated with DMSO (2 μmol/L), Oxa (2 μmol/L), APAP (2 μmol/L), OAP2 (2 μmol/L) were treated for 24 h. All cells were harvested and stained with Annexin V/PI Apoptosis Kit (Dojindo Laboratories, AD10) according to the manufacturer's instructions. Flow cytometry analysis (FC) was performed using a BD-FACSCelesta instrument. Finally, the flow cytometry data were prcessed using the flowjo X software.

4.10. Western blot

4T1 cells were seeded in a 6-well plate until reaching a confluency of approximately 70%. The cells were incubated with DMSO (2 μmol/L), Oxa (2 μmol/L), APAP (2 μmol/L), OAP2 (2 μmol/L) for 24 h. The proteins were extracted from cells using RIPA (Beyotime Biotechnology, P0013B) solution supplemented with PMSF (Beyotime Biotechnology, ST505) and Phosphatase inhibitor cocktail A (Beyotime Biotechnology, P1081). Subsequently, the proteins were separated using SDS-PAGE (Beyotime Biotechnology, P0012AC) and transferred onto 0.45 μm PVDF membranes (Millipore, IPVH00010). The membranes were blocked with 5% non-fat powdered milk (Beyotime Biotechnology, P0216) in TBST for 1 h at room temperature. Primary

antibodies, including Bal-2 (CST, 3498, 1:1000), Bax (CST, 14796, 1:1000), Caspase-3 (CST, 14220, 1:1000), GAPDH (Abcam, ab215191, 1:10000), γ-H2AX (Abcam, ab81299, 1:5000), Sam50 (Proteintech, 67425-1-Ig, 1:5000), COX II (SANTA, k2421, 1:500), Bak (CST, 12105, 1:1000), STING (CST, 50494, 1:1000), P-STING (CST, 72971, 1:1000), TBK1 (CST, 3504, 1:1000), P-TBK1 (CST, 5483, 1:1000), IRF3 (CST, 4302, 1:1000), P-IRF3 (CST, 29047, 1:1000), cGAS (Abcam, ab302617, 1:1000), GSDMD (CST, 39754, 1:1000), Cleave-GSEDMD (CST, 10137, 1:1000), IL-1β (CST, 12507, 1:1000), Cleave-IL-1β (CST, 63124, 1:1000), Caspase-1 (CST, 24232, 1:1000), Cleaved Caspase-1 (CST, 89332, 1:1000), Vinculin (Abcam, ab129002, 1:50,000), NLRP3 (Abcam, ab263899, 1:1000), were incubated at 4 °C overnight. The membranes were then washed four times for 7 min in TBST and incubated with Goat Anti-Rabbit IgG H&L (HRP) (Abcam, ab205718, 1:10,000) and Goat Anti-Mouse IgG H&L (HRP) (Servicebio, GB23301, 1:3000) secondary antibodies for 1 h at room temperature. Finally, images were obtained using the Chemiluminescence Imaging System (VILBER−VILBER FUSION FX6.EDGE) with BeyoECL Star (Beyotime Biotechnology, P0018AM).

4.11. Caspase-3 activity detected assay

The GreenNuc™ Caspase-3 Assay Kit for Live Cells (Beyotime Biotechnology, C1168S) was used for staining the active caspase-3 of 4T1 cells. Cells were cultured on a glass slide in a 12-well plate until reaching a confluency of approximately 70%. The cells were incubated with DMSO (2 μmol/L), Oxa (2 μmol/L), APAP (2 μmol/L), OAP2 (2 μmol/L) for 24 h. Next, cells were stained with GreenNuc™ Caspase-3 (10 μmol/L) following the manufacturer's instructions and the results were analyzed by the CLSM.

4.12. Mitochondrial membrane potential test assay

Mitochondrial membrane potential was measured by the FC and CLSM. 4T1 cells were seeded in a 6-well plate or CLSM dishes, and cultured with DMSO (2 μmol/L), Oxa (2 μmol/L), APAP (2 μmol/L), OAP2 (2 μmol/L) for 24 h. The cells were then stained with an enhanced mitochondrial membrane potential assay kit with JC-1 (Beyotime Biotechnology, C2003) following the manufacturer's instructions.

4.13. RNA-seq analysis

4T1 cells were seeded in a 60 mm cell-culture dish and treated with DMSO (2 μmol/L), Oxa (2 μmol/L), APAP (2 μmol/L), OAP2 (2 μmol/L) for 24 h. Subsequently, the cells were collected and total RNA was extracted by Trizol (Thermo Fisher, 15596018) following the manufacturer's instructions. The RNA samples were then purified and quantified using the Bioanalyzer 2100 and RNA 6000 Nano LabChip Kit (Agilent, CA, USA, 5067-1511). High-quality RNA samples with an RNA Integrity Number (RIN) > 7.0 were selected for library constrction.

RNA-seq was performed by LC Sciences through the Illumina X10 platform (Hangzhou, China). The genes with the false discovery rate (FDR) parameter below 0.05 and an absolute fold change of at least 2 were considered differentially expressed genes (DEGs). Enrichment analysis of Gene Ontology (GO) functions and Kyoto Encyclopedia of Genes and Genomes (KEGG) pathways was performed on the DEGs. The correlation among all samples was detected using Pearson correlation analysis and principal component analysis (PCA). Volcano analysis was used to identify the DEGs between the treated and control groups.

4.14. Immunofluorescence staining

4T1 cells were seeded in 12-well plates until reaching a confluency of approximately 70%. Subsequently, the cells were treated with DMSO (2 μmol/L), Oxa (2 μmol/L), APAP (2 μmol/L), OAP2 (2 μmol/L) for 24 h. After the incubation period, the cells were washed 3 times with cold PBS and fixed with 4% paraformaldehyde for 10 min at room temperature. To permeabilize the cells, 0.2% Triton X-100 in PBS was applied for 5 min at room temperature. After that, the cells were blocked with 5% BSA (Sangon Biotech (Shanghai) Co., Ltd., A500023) in TBST for 0.5 h at room temperature. Primary antibodies were incubated at 4 °C overnight. After washing the cells 4 times with TBST, and the second antibodies were incubated for 1 h at room temperature. Finally, the nucleus was stained with 4,6-diamidino-2-phenylindole (DAPI, Invitrogen, R37606) or Hoechst 33342 (Beyotime Biotechnology, C1025). The antibodies and their working diluted concentrations were as follows: anti-DNA (PROGEN, 1:200), Sam50 (1:500), Bak (1:200), CRT (Abcam, ab215191, 1:500), HMGB1 (Abcam, ab79823, 1:250), Phospho-STING (CST, 62912, 1:400), CoraLite488-conjugated goat anti-rabbit IgG (H + L) (Proteintech, SA00013-2, 1:500), and Cy3-conjugated goat anti-mouse IgG (H + L) (Servicebio, GB21301, 1:500), Goat Anti-Mouse IgG H&L (Alexa Fluor® 647) pre-adsorbed (Abcam, ab150119, 1:1000).

4.15. ELISA

Cytokines secreted by cells or tumor tissues were measured using an ELISA assay. Cells and tumor tissue were extracted using ELISA lysis buffer at 4 °C. The samples were collected and stored at −80 °C until further analysis. The ELISA kit used in this study, including IFN-α (F31099), IFN-β (F2124), HMGB1 (F2828), IL-12 (F30084), IL-10 (F2176), IL-1β (F2040), TNF-α (F2132), IFN-γ (F2182), TGF-β (F2686), were purchased from Shanghai Fanke Industrial Co., Ltd.

4.16. ROS detection

2′,7′-Dichlorodihydrofluorescein diacetate (DCFH-DA), a ROS probe, was purchased from Beyotime Biotechnology (S0033S) and used to measure ROS generation in 4T1 cells. The cells were seeded in 6- or 12-well plates until reaching a confluency of approximately 70%. Subsequently, the cells were treated with DMSO (2 μmol/L), Oxa (2 μmol/L), APAP (2 μmol/L), OAP2 (2 μmol/L) for 24 h. After drug incubation, the cells were stained following the provided protocols, and the results were analyzed by FC and CLSM.

4.17. GSH detection

GSSG/GSH Quantification Kit II was purchased from Dojindo Laboratories (G263) and used to measure the concentration of GSH in 4T1 cells. The cells were seeded in 6-well plates until reaching a confluency of approximately 70%. Subsequently, the cells were treated with DMSO (2 μmol/L), Oxa (2 μmol/L), APAP (2 μmol/L), OAP2 (2 μmol/L) for 24 h. After drug incubation, the GSH concentration was measured following the provided

protocols, and the results were detected using a microwell plate multifunctional detector.

4.18. LDH detection

LDH Release Assay Kit was purchased from Beyotime Biotechnology (C0016) and used to measure the release of LDH in 4T1 cells. The cells were seeded in 6-well plates until reaching a confluency of approximately 70%. Subsequently, the cells were treated with DMSO (2 μmol/L), Oxa (2 μmol/L), APAP (2 μmol/L), OAP2 (2 μmol/L) for 24 h. After drug incubation, the LDH release assay was performed following the provided protocols, and the results were detected using a microplate multifunctional detector.

4.19. BMDCs activation in vitro

BMDCs were extracted from the femur and tibia of male c57 mice aged 6−8 weeks. The extracted BMDCs were seeded in 10 mm cell culture dishes and cultured in DMEM medium containing IL-4 (10 ng/mL) and GM-CSF (20 ng/mL). The culture medium was refreshed every two days. On the 7th day, the BMDCs were collected for subsequent experiments. Drug-treated 4T1 cells and BMDC were co-cultured in the 6-well plate. After 24 h, mature DC cells (CD11c+, CD80+, CD86+) were examined using FC.

4.20. Anti-tumor effect in vivo

Anti-tumor efficacy and safety were evaluated using a 4T1 subcutaneous tumor model. When the tumor volume reached approximately 50 mm^3 on the 7th day, the mice were randomly divided into five groups. Each group was treated with PBS (negative control), Oxa, APAP, Oxa plus APAP, and OAP2. The drugs were administered *via* intravenous injection every two days. The body weight and tumor volume of mice were regularly measured during the experiment. At the end of the experiment, the main organs and blood samples were collected to evaluate the safety of the drug.

4.21. Tumor immune activation in vivo

First, the orthotopic 4T1 mouse model was established. The tumor-bearing mice were randomly divided into 4 groups ($n = 6$) and subjected to interventions using PBS, Oxa, APAP, and OAP2. Following the treatment, all mice were euthanized, and samples were collected from the tumors, spleen and inguinal lymph nodes. The immune cell populations were measured using FC ($n = 3$). For the detection of immune cytokines, tumor tissues from treated mice were collected ($n = 3$). Cytokines were extracted using ELISA Cytokine Extraction Solution, and specific ELISA Kits were used for the assays as described in the manuscript. The following antibodies and kits were used in the flow cytometry and ELISA analyses: CoraLite® Plus 488 Anti-Mouse CD4, CoraLite®568 Anti-Mouse CD3, APC Anti-Mouse CD86, FITC Plus Anti-Mouse CD11c, and PE Anti-Mouse CD80 (B7-1) were purchased from Proteintech. CD8α (2.43) Rat mAb (PE Conjugate), CD16/CD32 (2.4G2) Rat mAb, and 7-AAD Cell Staining Solution were purchased from Cell Signaling Technology (CST). PE anti-mouse CD206, PerCP/Cyanine5.5 anti-mouse CD45 Antibody, FITC anti-mouse F4/80 Antibody, and Zombie Violet™ Fixable Viability Kit were purchased from BioLegend, Inc.

4.22. Anti-tumor metastasis model in vivo

We extablised two *in vivo* models to validate anti-tumor metastasis effects of OAP2, namely lung metastasis model and the bilateral tumor model. For the lung-metastatic mouse tumor model, 1×10^5 4T1 tumor cells were intravenously injected on the 7th day before drug treatment. The mice were divided into 4 groups. The tumor volume and weight changes were recorded during the experiments. On the 16th day, the mice were euthanized, and the lungs were stained with H&E for further analysis.

In the bilateral tumor model, the same procedure as described above was followed. The tumor changes on both sides were recorded during the experiment, and CD8 immunofluorescence staining was performed on the distal tumor after the experiment.

4.23. Statistical analysis

The data were presented as means SD. Two-sided unpaired *t*-tests were used to compare statistical differences between groups. One-way ANOVA with Tukey's multiple comparisons was used to examine statistical differences for studies of multiple samples. The statistical analysis program GraphPad Prism version 9 was used for all calculations. The statistical significant was determined using a cutoff of $P<0.05$. Significant levels were denoted by the following symbols: $^*P<0.05$, $^{**}P<0.01$, $^{***}P<0.001$ and $^{****}P<0.0001$.

Acknowledgments

This work was supported by the National Natural Science Foundation of China (82173682, China), Shenzhen Science and Technology Program (JCYJ20210324133213037, China), Innovation Capability Support Program of Shaanxi (2021KJXX-92, China). Thanks to Prof. Qiuhua Luo (China Medical University, Shenyang, China) for her help with the language of the manuscript.

Author contributions

Conceptualization: Gaofei Wei, Yang Liu, Maosheng Cheng. Methodology: Renming Fan, Ruizhuo Lin, Shuo Zhang, Aohua Deng, Yongrui Hai, Junyan Zhuang. Writing-origin draft: Renming Fan. Writing-review & editing: All authors.

Conflicts of interest

The authors declare no conflict of interest.

Appendix A. Supporting information

Supporting information to this article can be found online at https://doi.org/10.1016/j.apsb.2023.11.032.

References

1. Vyas S, Zaganjor E, Haigis MC. Mitochondria and cancer. *Cell* 2016; **166**:555−66.
2. Vasan K, Werner M, Chandel NS. Mitochondrial metabolism as a target for cancer therapy. *Cell Metabol* 2020;**32**:341−52.

3. Porporato PE, Filigheddu N, Pedro JMB, Kroemer G, Galluzzi L. Mitochondrial metabolism and cancer. *Cell Res* 2018;**28**:265−80.
4. Zielonka J, Joseph J, Sikora A, Hardy M, Ouari O, Vasquez-Vivar J, et al. Mitochondria-targeted triphenylphosphonium-based compounds: syntheses, mechanisms of action, and therapeutic and diagnostic applications. *Chem Rev* 2017;**117**:10043−120.
5. Mills EL, Kelly B, O'Neill LAJ. Mitochondria are the powerhouses of immunity. *Nat Immunol* 2017;**18**:488−98.
6. Spinelli JB, Haigis MC. The multifaceted contributions of mitochondria to cellular metabolism. *Nat Cell Biol* 2018;**20**:745−54.
7. West AP, Shadel GS. Mitochondrial DNA in innate immune responses and inflammatory pathology. *Nat Rev Immunol* 2017;**17**:363−75.
8. Enzan N, Matsushima S, Ikeda S, Okabe K, Ishikita A, Yamamoto T, et al. ZBP1 protects against mtDNA-induced myocardial inflammation in failing hearts. *Circ Res* 2023;**132**:1110−26.
9. Wang Y, Patti GJ. The warburg effect: a signature of mitochondrial overload. *Trends Cell Biol* 2023;**33**:1014−20.
10. Icard P, Shulman S, Farhat D, Steyaert JM, Alifano M, Lincet H. How the warburg effect supports aggressiveness and drug resistance of cancer cells?. *Drug Resist Updates* 2018;**38**:1−11.
11. Zhong X, He X, Wang Y, Hu Z, Huang H, Zhao S, et al. Warburg effect in colorectal cancer: the emerging roles in tumor microenvironment and therapeutic implications. *J Hematol Oncol* 2022;**15**:160.
12. Guo X, Yang N, Ji W, Zhang H, Dong X, Zhou Z, et al. Mito-Bomb: targeting mitochondria for cancer therapy. *Adv Mater* 2021;**33**:e2007778.
13. Li Z, Zou J, Chen X. In response to precision medicine: current subcellular targeting strategies for cancer therapy. *Adv Mater* 2022;**35**:e2209529.
14. Pan L, Liu J, Shi J. Cancer cell nucleus-targeting nanocomposites for advanced tumor therapeutics. *Chem Soc Rev* 2018;**47**:6930−46.
15. Yang Z, Wang L, Yang C, Pu S, Guo Z, Wu Q, et al. Mitochondrial membrane remodeling. *Front Bioeng Biotechnol* 2021;**9**:786806.
16. Faelber K, Dietrich L, Noel JK, Wollweber F, Pfitzner AK, Muhleip A, et al. Structure and assembly of the mitochondrial membrane remodelling GTPase Mgm1. *Nature* 2019;**571**:429−33.
17. Chen L, Dong J, Liao S, Wang S, Wu Z, Zuo M, et al. Loss of Sam50 in hepatocytes induces cardiolipin-dependent mitochondrial membrane remodeling to trigger mtDNA release and liver injury. *Hepatology* 2022;**76**:1389−408.
18. Bagchi S, Yuan R, Engleman EG. Immune checkpoint inhibitors for the treatment of cancer: clinical impact and mechanisms of response and resistance. *Annu Rev Pathol* 2021;**16**:223−49.
19. Zhu X, Li S. Nanomaterials in tumor immunotherapy: new strategies and challenges. *Mol Cancer* 2023;**22**:94.
20. Propper DJ, Balkwill FR. Harnessing cytokines and chemokines for cancer therapy. *Nat Rev Clin Oncol* 2022;**19**:237−53.
21. Man X, Yang T, Li W, Li S, Xu G, Zhang Z, et al. Developing a Gadolinium(III) compound based on apoferritin for targeted magnetic resonance imaging and dual-modal therapy of cancer. *J Med Chem* 2023;**66**:7268−79.
22. Zhao Z, Wang X, Wang J, Li Y, Lin W, Lu K, et al. A nanobody−bioorthogonal catalyst conjugate triggers spatially confined prodrug activation for combinational chemo-immunotherapy. *J Med Chem* 2023;**66**:11951−64.
23. Wang B, Tang D, Karges J, Cui M, Xiao H. A NIR-II fluorescent polybodipy delivering cationic Pt-NHC with type II immunogenic cell death for combined chemotherapy and photodynamic Immunotherapy. *Adv Funct Mater* 2023;**33**:2214824.
24. Qiao H, Chen Z, Fu S, Yu X, Sun M, Zhai Y, et al. Emerging platinum(0) nanotherapeutics for efficient cancer therapy. *J Control Release* 2022;**352**:276−87.
25. Zhang C, Xu C, Gao X, Yao Q. Platinum-based drugs for cancer therapy and anti-tumor strategies. *Theranostics* 2022;**12**:2115−32.
26. Li W, Li S, Xu G, Man X, Yang T, Zhang Z, et al. Developing a ruthenium(III) complex to trigger gasdermin E-mediated pyroptosis and an immune response based on decitabine and liposomes: targeting inhibition of gastric tumor growth and metastasis. *J Med Chem* 2023;**66**:13072−85.
27. Li X, Wang H, Chen Y, Li Z, Liu S, Guan W, et al. Novel emerging nano-assisted anti-cancer strategies based on the STING pathway. *Acta Materia Medica* 2023;**2**:323−41.
28. Hopfner KP, Hornung V. Molecular mechanisms and cellular functions of cGAS-STING signalling. *Nat Rev Mol Cell Biol* 2020;**21**:501−21.
29. Kwon J, Bakhoum SF. The cytosolic DNA-sensing cGAS-STING pathway in cancer. *Cancer Discov* 2020;**10**:26−39.
30. Zhang L, Wang Y, Karges J, Tang D, Zhang H, Zou K, et al. Tetrahedral DNA nanostructure with interferon stimulatory DNA delivers highly potent toxins and activates the cGAS-STING pathway for robust chemotherapy and immunotherapy. *Adv Mater* 2023;**35**:2210267.
31. White MJ, McArthur K, Metcalf D, Lane RM, Cambier JC, Herold MJ, et al. Apoptotic caspases suppress mtDNA-induced STING-mediated type I IFN production. *Cell* 2014;**159**:1549−62.
32. Lawrence G, Holley CL, Schroder K. Come on mtDNA, light my fire. *Immunity* 2022;**55**:1331−3.
33. Zecchini V, Paupe V, Herranz-Montoya I, Janssen J, Wortel IMN, Morris JL, et al. Fumarate induces vesicular release of mtDNA to drive innate immunity. *Nature* 2023;**615**:499−506.
34. Fan R, Deng A, Qi B, Zhang S, Sang R, Luo L, et al. CJ(2): a novel potent platinum(IV) prodrug enhances chemo-immunotherapy by facilitating PD-L1 degradation in the cytoplasm and cytomembrane. *J Med Chem* 2023;**66**:875−89.
35. Hu M, Zhou M, Bao X, Pan D, Jiao M, Liu X, et al. ATM inhibition enhances cancer immunotherapy by promoting mtDNA leakage and cGAS/STING activation. *J Clin Invest* 2021;**131**:e139333.
36. Gao X, Lei G, Wang B, Deng Z, Karges J, Xiao H, et al. Encapsulation of platinum prodrugs into PC7A polymeric nanoparticles combined with immune checkpoint inhibitors for therapeutically enhanced multimodal chemotherapy and immunotherapy by activation of the STING pathway. *Adv Sci* 2023;**10**:e2205241.
37. Ling YY, Xia XY, Hao L, Wang WJ, Zhang H, Liu LY, et al. Simultaneous photoactivation of cGAS-STING pathway and pyroptosis by platinum(II) triphenylamine complexes for cancer immunotherapy. *Angew Chem Int Ed* 2022;**61**:e202210988.
38. Cao L, Tian H, Fang M, Xu Z, Tang D, Chen J, et al. Activating cGAS-STING pathway with ROS-responsive nanoparticles delivering a hybrid prodrug for enhanced chemo-immunotherapy. *Biomaterials* 2022;**290**:121856.
39. McArthur K, Whitehead LW, Heddleston JM, Li L, Padman BS, Oorschot V, et al. BAK/BAX macropores facilitate mitochondrial herniation and mtDNA efflux during apoptosis. *Science* 2018;**359**:eaao6047.
40. Hayes JD, Dinkova-Kostova AT, Tew KD. Oxidative stress in cancer. *Cancer Cell* 2020;**38**:167−97.
41. Pu Y, Zhou B, Xiang H, Wu W, Yin H, Yue W, et al. Tyrosinase-activated prodrug nanomedicine as oxidative stress amplifier for melanoma-specific treatment. *Biomaterials* 2020;**259**:120329.
42. Gai C, Yu M, Li Z, Wang Y, Ding D, Zheng J, et al. Acetaminophen sensitizing erastin-induced ferroptosis *via* modulation of Nrf2/heme oxygenase-1 signaling pathway in non-small-cell lung cancer. *J Cell Physiol* 2020;**235**:3329−39.
43. Pang X, He X, Qiu Z, Zhang H, Xie R, Liu Z, et al. Targeting integrin pathways: mechanisms and advances in therapy. *Signal Transduct Targeted Ther* 2023;**8**:1.
44. Wu Y, Yang Z, Cheng K, Bi H, Chen J. Small molecule-based immunomodulators for cancer therapy. *Acta Pharm Sin B* 2022;**12**:4287−308.
45. Zhang Y, Zhang Z. The history and advances in cancer immunotherapy: understanding the characteristics of tumor-infiltrating immune cells and their therapeutic implications. *Cell Mol Immunol* 2020;**17**:807−21.